

GPS-Aided Deep Learning for Beam Prediction and Tracking in UAV mmWave Communication

Vendi Ardianto Nugroho and Byung Moo Lee, *Senior Member, IEEE*

Abstract—Millimeter-wave (mmWave) communication enables high data rates for cellular-connected Unmanned Aerial Vehicles (UAVs). However, a robust beam management remains challenging due to significant path loss and the dynamic mobility of UAVs, which can destabilize the UAV-base station (BS) link. This research presents a GPS-aided deep learning (DL) model that simultaneously predicts current and future optimal beams for UAV mmWave communications, maintaining a Top-1 prediction accuracy exceeding 70% and an average power loss below 0.6 dB across all prediction steps. These outcomes stem from a proposed data set splitting method ensuring balanced label distribution, paired with a GPS preprocessing technique that extracts key positional features, and a DL architecture that maps sequential position data to beam index predictions. The model reduces overhead by approximately 93% (requiring the training of 2 ~ 3 beams instead of 32 beams) with 95% beam prediction accuracy guarantees, and ensures 94% to 96% of predictions exhibit mean power loss not exceeding 1 dB.

Index Terms—Millimeter wave communication, GPS, drone, UAV, deep learning, beam prediction, beam tracking.

I. INTRODUCTION

Unmanned Aerial Vehicles (UAV) are expected to serve two roles in wireless networks both as user equipment (UE) that accesses cellular network (cellular-connected UAV) and as UAV-assisted communication platforms providing aerial base stations (BS) and relays for terrestrial users [1]. Enabling millimeter wave (mmWave) in cellular-connected UAVs could support ultra high data traffic and various UAV applications such as aerial surveillance and disaster rescue due to the broad bandwidth in the mmWave frequency band [2]. As the high path loss characteristic of mmWave, deploying large antenna arrays on the BS side helps mitigate it by generating narrow beams with strong beamforming gains [3]. As a result, mmWave communications rely heavily on efficient beam management—including beam training and tracking—to quickly select the appropriate beams during intra- and inter-cell mobility, minimizing the risk of beam misalignment [4]. Moreover, UAV's high mobility introduces uncertainty in parameters like velocity and acceleration, necessitating the development of dedicated beam management methods tailored for UAV systems [5]. This highlights the need for innovative approaches to overcome this challenge and enable high-speed mmWave communication for UAV-assisted cellular networks.

In mmWave communication systems, maintaining user connectivity relies on two key steps: initial access and beam

tracking [6], [7]. The initial access phase establishes the first connection between BS and UE through beam training algorithms. Once the initial beam direction is set, beam tracking algorithms take over to maintain directional communication quality and accelerate subsequent beam adjustments as the user moves. The key challenges in beam management include high overhead during the beam training process and maintaining beam alignment under UE mobility, which can significantly impact system performance. To tackle these challenges, researchers have proposed numerous approaches aimed at minimizing training overhead and improving the effectiveness of beam tracking systems.

Focusing first on the initial access phase, researchers have developed multiple approaches to reduce beam training overhead through various techniques [8–13]. One method involves hierarchical beam searching, as demonstrated by [8] and [9], which employs multi-layer codebooks where higher layers utilize increasingly narrow beams, thus eliminating the need for comprehensive narrow-beam combination searches. Another approach focuses on compressive channel estimation [10, 11], which aims to identify the strongest multi-path components Angle of Arrival (AoA) and Angle of Departure (AoD) pairs. Alternative solutions have emerged through deep learning (DL) applications, including the approach of using pilot signals received by multiple BS in [12], and method of combining instantaneous mmWave wide beam signals with sub-6 GHz Channel State Information (CSI) for optimal beam estimation in [13]. While these beam training approaches provide initial beam alignment, maintaining optimal beam pairs during user mobility requires effective beam tracking solutions.

Various beam tracking solutions have been proposed in the literature [14–18]. The study in [14] developed an Extended Kalman Filter (EKF) solution, while research in [15] implemented an Unscented Kalman Filter (UKF) to sustain communication links. Taking a different approach, research in [16] introduced a Gaussian process-based machine learning framework that enables swift and precise UAV position prediction with measurable uncertainty levels. This prediction helps constrain beam-tracking to specific spatial areas around the predicted UAV positions. The study in [17] focused on predicting angles between UAV-mounted BS and UE, enabling both components to configure their transmit and receive beams beforehand, thus enhancing communication reliability. Whereas the study in [18] concentrated on UAV location prediction, using the forecasted positions to determine optimal angles between UAV and BS, facilitating efficient beam alignment for subsequent time slots.

Building upon these advances in beam training and tracking,

The authors are with the Department of Intelligent Mechatronics Engineering, and Department of Convergence Engineering for Intelligent Drone, Sejong University, Seoul, 05006, South Korea, (e-mail: vendi@sju.ac.kr; blee@sejong.ac.kr).

researchers explored sensing-aided DL approaches that leverage sensor data to further improve performance [19–22]. The authors in [19] utilized Global Positioning System (GPS) data and applied a Multi Layer Perceptron (MLP) model, while the study in [21] combines GPS and vision data to perform current beam prediction. A Recurrent Neural Network (RNN) based model was employed using LiDAR [20], vision [23], and radar [22] to facilitate beam tracking. While these approaches are effective to predict several future beams, these works are designed for vehicle-to-infrastructure (V2I) and vehicle-to-vehicle (V2V) scenarios which have different movement characteristics compared to UAV.

Recent research has focused on the challenges of beam management in UAV communications [24–28]. The research in [24] applied a Convolutional Neural Network (CNN) and MLP models using GPS and image modalities for beam prediction, while studies in [25–27] focused on image data with DL models for the same purpose. However, due to UAV’s rapid movements, current beam predictions may become outdated during data processing, making future beam prediction essential for stable connectivity. The research presented in [28] introduced DL models for beam prediction and tracking, utilizing GPS and visual data for UAV communications. However, this approach needs separate models for the current and future beam predictions which may increase computational overhead. Additionally, while GPS-based prediction is crucial when visual sensing fails (e.g., in low light), its performance lags behind vision-based and beam vector-based DL models. These challenges motivated our development of a GPS-based DL model capable of simultaneous current and future beam prediction for UAV communications.

This paper presents a lightweight GPS-based approach for mmWave beam prediction and tracking. The key contributions of this work include:

- Designed a GPS-aided DL model architecture that simultaneously performs beam prediction and tracking in UAV mmWave communication scenario, leveraging real-world GPS data from DeepSense6G data set [29].
- Proposed a data set splitting strategy called *adjusted splitting* to ensure similar data distribution in training, validation, and test sets.
- Proposed a GPS data preprocessing method that combine normalized UE’s geodetic position with UE-BS unit vector to obtain optimal beam prediction and tracking performance.

The rest of this paper is organized as follows. Section II presents the system model and the proposed solution. In Section III, the evaluation setup is introduced. In Section IV, the evaluation result is discussed. Finally, Section V concludes the paper.

Notations: In this paper, boldface lower-case letters denote vectors. For a vector \mathbf{h} , its Hermitian transpose is denoted as \mathbf{h}^H . $\mathbb{C}^{Q \times 1}$ denotes the space of $Q \times 1$ complex-valued vectors. $\mathbb{E}[\cdot]$ denotes the expectation operator, and $\mathbb{P}\{\cdot\}$ represents probability. For a position vector \mathbf{g} , ϕ and λ denote latitude and longitude respectively. For time series data, $[t]$ denotes the value at time step t , and a sequence of W consecutive observations is denoted as $\{[t - W + 1], \dots, [t]\}$, where W

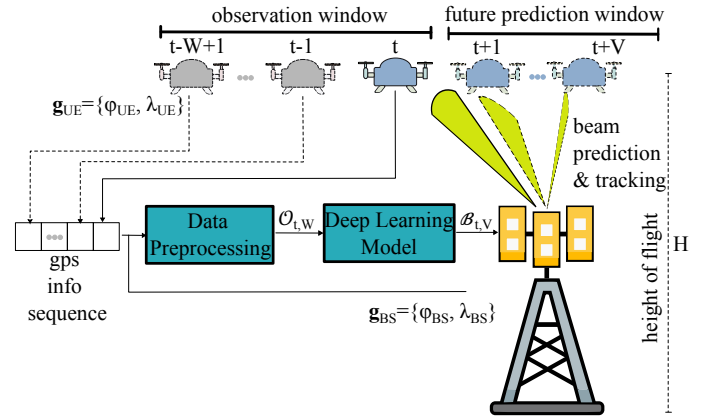


Fig. 1: System Architecture

represents the observation window size. Predictions with step v are denoted as $[t + v]$, where $v \in \{0, \dots, V\}$ and V is the maximum prediction step. $\mathcal{F} = \{\mathbf{f}_m\}_{m=1}^M$ denotes the beam codebook with M beam vectors. \mathbf{u}_{UE-BS} represents the unit vector between UE and BS positions.

II. SYSTEM MODEL AND PROPOSED SOLUTION

This section commences by presenting the underlying system model that forms the foundation of our research. We then outline the specific beam management tasks we address including GPS-aided current beam prediction and future beam prediction. We then proceed to present our proposed solution.

A. System Model

The system architecture, depicted in Figure 1, focuses on the communication link between a UAV-mounted single antenna (UE) and a BS equipped with Q antennas. The BS employs beamforming using vectors selected from its codebook $\mathcal{F} = \{\mathbf{f}_m\}_{m=1}^M$, where each $\mathbf{f}_m \in \mathbb{C}^{Q \times 1}$ and M is the total number of beamforming vectors. This formulation includes beamforming at the BS, considering Time Division Duplexing (TDD) to facilitate the use of same frequency bands for both uplink and downlink transmissions. For an illustration, at time step t , when the BS transmits a complex symbol $x[t] \in \mathbb{C}$ using a beam vector $\mathbf{f}[t]$, the received symbol at the UE can be expressed as:

$$y[t] = \mathbf{h}^H[t] \mathbf{f}[t] x[t] + n[t]. \quad (1)$$

In this expression, $\mathbf{h}[t] \in \mathbb{C}^{Q \times 1}$ denotes the complex wireless channel between the BS and UE antennas at time t . The downlink signal $x[t]$ complies with power constraint $\mathbb{E}[x[t]^H x[t]] = P$, where P denotes the transmit power. The term $n[t]$ is the receive noise which satisfies $\mathbb{E}[n[t] n^H[t]] = \sigma_n^2$, where σ_n^2 represents the receive noise power.

B. Problem Formulation and DL Task Definitions

This study adopts the problem formulation and DL task definitions from [23] and [20] to define the optimal beam vector and index, as well as the beam prediction and beam

tracking tasks. The BS achieves optimal beam selection by choosing the beam vector \mathbf{f} that generates the highest received power. The ideal beam vector $\mathbf{f}^*[t]$ is expressed as:

$$\mathbf{f}^*[t] = \underset{\mathbf{f}[t] \in \mathcal{F}}{\operatorname{argmax}} |\mathbf{h}^H[t] \mathbf{f}[t]|^2. \quad (2)$$

Under this pre-defined codebook constraint, the optimal beam vector $\mathbf{f}^*[t]$ can be uniquely identified by its corresponding beam index within the codebook. At time step t , the optimal beam index $b^*[t]$ is determined by the following condition:

$$b^*[t] = \underset{b[t] \in \{1, 2, \dots, M\}}{\operatorname{argmax}} |\mathbf{h}^H[t] \mathbf{f}_{b[t]}|^2, \quad (3)$$

where M represents the size of codebook \mathcal{F} and $\mathbf{f}_{b[t]}$ represents the $b[t]$ -th beam vector from the codebook \mathcal{F} at time t . It is worth emphasizing that under the codebook constraint, determining the optimal beam is equivalent to identifying its corresponding optimal beam index.

This study investigates utilizing UAV positional information to enable beam prediction (estimating current beams) and beam tracking (forecasting future beams). The two-dimensional position vector at time t , represented as $\mathbf{g}_{UE, norm}[t] \in \mathbb{R}^2$, consists of UE's normalized latitude $\phi_{UE, norm}[t]$ and longitude $\lambda_{UE, norm}[t]$. Additionally, $\mathbf{u}_{UE-BS}[t] \in \mathbb{R}^3$ is defined as a unit vector derived from the positions of the UE and BS at time t . Further details on the definitions of $\mathbf{g}_{UE, norm}[t]$ and $\mathbf{u}_{UE-BS}[t]$ are provided in subsection II-C1.

To predict both current and future beams, these representations are combined as $\mathbf{O}[t] = \{\mathbf{g}_{UE, norm}[t], \mathbf{u}_{UE-BS}[t]\}$. The sequence of observed sensory data within an observation window $W \in \mathbb{Z}^+$ is defined as $\mathcal{O}_{t,W} = \{\mathbf{O}[t-W+1], \dots, \mathbf{O}[t]\}$. Using the definition of the optimal beam index provided in equation

$$\max_{\hat{\mathcal{B}}_{t,V}} \mathbb{P}\{\hat{\mathcal{B}}_{t,V} = \mathcal{B}_{t,V}^* | \mathcal{O}_{t,W}\}. \quad (4)$$

In this context, $\mathbb{P}\{\cdot | \cdot\}$ denotes the conditional probability. The term $\hat{\mathcal{B}}_{t,V}$ represents the predicted beam index $b[t]$ sequence starting from time step t to $t+V$, the term $\mathcal{B}_{t,V}^*$ represents the optimal beam index $b^*[t]$ sequence starting from time step t to $t+V$, while $\mathcal{O}_{t,W}$ refers to the observed sensory data from time step $t-W+1$ through t . Furthermore, $v \in \{0, 1, 2, \dots, V\}$ represents the prediction step in the beam prediction and tracking process. Below, we provide a formal definition of the DL task for beam prediction and tracking.

Beam Prediction and Tracking DL Task Definition: In this approach, we use a DL model to solve equation (4). To address the beam prediction problem, the goal of the DL model is to predict the optimal beam index sequence $\mathcal{B}_{t,V}^*$ based on the sensory data sequence $\mathcal{O}_{t,W}$. Consequently, the optimal DL model for GPS-aided beam prediction and tracking can be expressed as:

$$f_{bpt}^*(\mathcal{O}_{t,W}; \Theta_{bpt}^*) = \underset{f_{bpt}(\cdot), \Theta_{bpt}}{\operatorname{argmax}} \mathbb{P}\{f_{bpt}(\mathcal{O}_{t,W}; \Theta_{bpt}) = \mathcal{B}_{t,V}^*\}, \quad (5)$$

where $f_{bpt}^*(\cdot)$ represents the DL optimal model's mapping function for the beam prediction and tracking task, and Θ_{bpt}^* refers to the optimal model's training parameters.

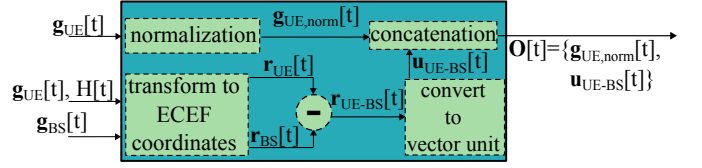


Fig. 2: GPS data preprocessing pipeline for the proposed beam prediction and tracking system

C. Proposed Solution

In this subsection, we introduce how the GPS data being processed before used as the DL model input and the architecture of DL model.

1) *GPS Data Preprocessing:* Given that raw GPS sequence data implicitly encodes spatiotemporal information, preprocessing is essential before inputting the data into a DL model to achieve optimal performance [30]. The block diagram in Figure 2 block illustrates our approach to preprocess GPS data collected from UE and BS. Initially, we normalize the UE's position using min-max normalization. Subsequently, we transform geodetic coordinates to Earth-centered Earth-fixed (ECEF) coordinates and extract the UE-BS vector unit. The final step involves concatenating these features. In the following sections, we elaborate on the min-max normalization process and the technique for obtaining ECEF coordinates.

a)

- 1) **Min-max Normalization:** Consider a data set \mathcal{D} comprising K sample pairs of UE's latitude and longitude $\mathbf{g}_{UE,k} = (\phi_{UE,k}, \lambda_{UE,k})_{k=1}^K$. We identify $\phi_{UE,min}$ and $\phi_{UE,max}$ as the minimum and maximum latitude values in data set \mathcal{D} , and $\lambda_{UE,min}$ and $\lambda_{UE,max}$ as the minimum and maximum longitude values. The normalization process transforms each UE's latitude and longitude to a value between 0 and 1 using the following equations:

$$\phi_{UE, norm, k} = \frac{\phi_{UE, k} - \phi_{UE, min}}{\phi_{UE, max} - \phi_{UE, min}}, \quad (6)$$

$$\lambda_{UE, norm, k} = \frac{\lambda_{UE, k} - \lambda_{UE, min}}{\lambda_{UE, max} - \lambda_{UE, min}}, \quad (7)$$

- 2) **ECEF Coordinate Transformation:** Drawing from Paul's work in [31] as referenced in [32], the ECEF coordinates (α, β, γ) of a point \mathbf{r} can be computed from its geodetic coordinates (ϕ, λ, A) using the following mathematical transformations:

$$\alpha = (R + A) \cos \phi \cos \lambda, \quad (8)$$

$$\beta = (R + A) \cos \phi \sin \lambda, \quad (9)$$

$$\gamma = (R + A - e^2 R) \sin \phi, \quad (10)$$

where

$$R = \frac{a}{\sqrt{1 - e^2 \sin^2 \phi}}. \quad (11)$$

The parameters in these equations represent: ϕ as geodetic latitude, λ as geodetic longitude, A as the altitude normal to the ellipsoid, a as the ellipsoidal equatorial radius ($a = 6378.137$ km for WGS-84 model), and e as the ellipsoid's eccentricity ($e^2 = 0.00669437999$ for WGS-84 model). We define $\mathbf{r}_{BS}[t]$ and $\mathbf{r}_{UE}[t]$ as the

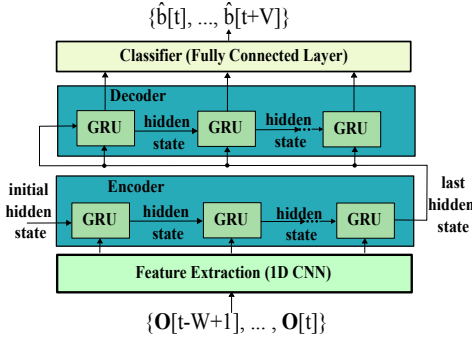


Fig. 3: Neural network architecture used for beam prediction and tracking

ECEF coordinates of BS and UE at time t respectively. The UE-BS vector $\mathbf{r}_{UE-BS}[t]$ is expressed as:

$$\mathbf{r}_{UE-BS}[t] = \mathbf{r}_{UE}[t] - \mathbf{r}_{BS}[t]. \quad (12)$$

With the magnitude of $\mathbf{r}[t]$ is calculated as $|\mathbf{r}[t]| = \sqrt{\alpha^2 + \beta^2 + \gamma^2}$, we express the unit vector of the UE-BS vector $\mathbf{u}_{UE-BS}[t]$ as:

$$\mathbf{u}_{UE-BS}[t] = \frac{\mathbf{r}_{UE-BS}[t]}{|\mathbf{r}_{UE-BS}[t]|}. \quad (13)$$

2) *DL Model Architecture*: As illustrated in Figure 3, the proposed DL model architecture consists of three primary components: the Feature Extraction Block, the Encoder-Decoder RNN Block, and the Classifier Block. Since 1D CNNs excel at extracting meaningful features from sequential data [33], the feature extraction block utilizes 1D CNN layers to process GPS sequence data $\mathcal{O}_{t,W}$, facilitating the detection of UAV movement patterns. The kernel size is configured to 3 to capture local features over each 3 of time steps, while the kernel advances with a stride of 1 for ensuring detailed coverage. To maintain the original sequence length post-feature extraction, we add zero padding at both the start and end of the input data. Table I provides a comprehensive overview of the network architecture and its parameters. It specifies the input and output feature channels (c_i and c_o respectively), alongside the kernel size, stride, and padding parameters (k_1, k_2, k_3). The architecture incorporates batch normalization (BN) layers to standardize the data distribution to zero mean and unit variance.

The encoder-decoder RNN architecture uses two RNNs: an encoder that compresses a variable-length input sequence into a fixed-dimensional context vector, and a decoder that generates a variable-length output sequence from this vector [34]. Since this architecture can effectively transform sequences (e.g., for language translation), we adapt it to predict beam index sequence from GPS sequence. Our encoder processes a W -step GPS sequence, capturing temporal dependencies through hidden state updates, while the decoder autoregressively produces the corresponding $V + 1$ -step beam index sequence. Since GRUs offer superior convergence properties over standard RNNs as demonstrated in [35], we implement GRU in both the encoder and decoder.

The classifier block consists of two fully connected (FC) layers with a softmax activation function to predict current optimal beam index and future beam index $\hat{\mathcal{B}}_{t,V} =$

TABLE I: Structure and parameters of the proposed network

Module	Layer	Parameter
Feature Extraction	1D Convolution	$c_i=5, c_o=128, (3,1,1)$
	1D Convolution	$c_i=128, c_o=128, (3,1,1), \text{BN}$
	ReLU Activation	$c_i=128, c_o=128$
Encoder	GRU	$c_i=128, c_o=128$
Decoder	GRU	$c_i=128, c_o=128$
Classifier	FC	$c_i=128, c_o=64$
	ReLU Activation	$c_i=64, c_o=64$
	FC	$c_i=64, c_o=32$
	Softmax Activation	$c_i=32, c_o=32$

$\{\hat{b}[t], \dots, \hat{b}[t+V]\}$. This approach generates a score vector $\hat{\mathbf{c}} = [c_1, \dots, c_M]^T$, where each score $c_m \in (0, 1)$ corresponds to a specific m -th beam b_m in the codebook. The optimal future beam is determined by selecting the beam index with the highest score

$$\hat{b} = \underset{b \in \{1, \dots, M\}}{\operatorname{argmax}} c_b. \quad (14)$$

Learning Process: The DL model undergoes offline supervised training, with each data point structured in two key components : (i) an input sequence of position data $\{\mathcal{O}[t-W+1], \dots, \mathcal{O}[t]\}$, and (ii) a label/desired output sequence $\{\mathbf{c}^*[t], \dots, \mathbf{c}^*[t+V]\}$ where each $\mathbf{c}^*[t+v]$ is a one-hot representation of $b^*[t+v]$. To address the classification problem, we implement a cross-entropy loss function focused on the last $V + 1$ outputs of the sequence. For each sample in the data set, the loss function is mathematically expressed as

$$\mathcal{L} = - \sum_{j=t}^{t+V} \sum_{m=1}^M b_m^*[j] \log_e(\hat{c}_m[j]), \quad (15)$$

where $b_m^*[j]$ denotes the m -th element of the one-hot coded vector \mathbf{b}^* at time step j , and $\hat{c}_m[j]$ represents the m -th element of the output vector $\hat{\mathbf{c}}[j]$ at the same time step. The loss for each sample is subsequently averaged across the entire data set. The training is configured with specific hyperparameters: 20 epochs, a train batch size of 8, a validation batch size of 1024, a test batch size of 1024, an Adam optimizer with a learning rate of 5×10^{-4} , a zero weight decay, and a learning rate reduction factor of 0.1 on epoch 12 and 18.

III. EVALUATION SETUP

This study leverages Scenario 23 from the DeepSense 6G data set [29] to investigate high-frequency wireless communication applications involving drones. The BS is configured with a 16-element phased array operating in the 60 GHz frequency band, utilizing a codebook comprising 32 predefined beams ($M = 32$). The UE takes the form of a remotely controlled drone equipped with a mmWave transmitter, a GPS receiver, and inertial measurement units (IMU). The transmitter features a quasi-omnidirectional antenna that continuously broadcasts signals omnidirectionally at the 60 GHz frequency band. Note that this study assumes uplink/downlink reciprocity in received power, as mmWave signals typically follow a dominant single path carrying most of the power. In the subsequent sections, we will elaborate on the data splitting

methodology and data transformation techniques employed to prepare the data set for our DL model.

A. Data Set Splitting Method

We consider a raw data set D_{raw} comprises K samples $D_{raw} = \{(q_k, t_k, \phi_{BS,k}, \lambda_{BS,k}, \phi_{UE,k}, \lambda_{UE,k}, H_k, \mathbf{u}_{UE-BS,k}, b_k^*)\}_k^K$, which encapsulate various key parameters. These parameters include the sequence index q , sample index t , BS's geodetic coordinates $(\phi_{BS,k}, \lambda_{BS,k})$, UE's geodetic coordinates $(\phi_{UE,k}, \lambda_{UE,k})$, the vertical distance between the drone and ground H_k , the UE-BS unit vector $\mathbf{u}_{UE-BS,k}$, and the actual beamforming index b_k^* . Note that the sequence index q is a label that groups together all the data samples collected during a single trip of the UE as it moves in front of the BS [29].

Employing equations (6) and (7), we normalize the UE's positioning. To calculate the UE-BS unit vector $\mathbf{u}_{UE-BS,k}$ with (13), first we determine the UE's ECEF coordinates using (12), where the UE's altitude is set to H_k and the BS's altitude to 0. The raw data set D_{raw} is subsequently partitioned into three distinct subsets: training (D_{raw}^{train}), validation (D_{raw}^{val}), and testing (D_{raw}^{test}) data sets, allocated according to predetermined percentage portions. Within each split data set, samples are arranged in ascending order based on their sample index t_k . Our objective is to compare two different data splitting strategy methods.

1) *Sequential Splitting*: We employ a straightforward method that preserves the original sample index order by sequentially partitioning D_{raw} . Specifically, the first 65% of D_{raw} becomes D_{raw}^{train} , the next 15% becomes D_{raw}^{val} , and the remaining 20% becomes D_{raw}^{test} .

2) *Adjusted Splitting*: In this approach, we split D_{raw} by considering the label distribution (optimal beam index b^*) through Algorithm 1. The primary goal is to ensure that the label distribution of each split data set reflects the label distribution of the original data set D_{raw} and follows the desired splitting percentage. The methodology unfolds through multiple stages: (i) We first divide the raw data set D_{raw} into multiple chunks. Each chunk is divided into train chunk data set D_{chunk}^{train} , validation chunk data set D_{chunk}^{val} , and test chunk data set D_{chunk}^{test} , which are then aggregated to form D_{raw}^{train} , D_{raw}^{val} , and D_{raw}^{test} . Recognizing that simple grouping might not guarantee the desired label distribution, we introduce an additional refinement. (ii) We organize split data sets into label-based grouped data sets $D_{group} = \{D_b\}_b^M$, where b represents the label (optimal beam index). Within each D_b , we implement a consistent 65%, 15%, and 20% split into train D_b^{train} , validation D_b^{val} , and test D_b^{test} data sets. We then consolidate all D_b^{train} into D_{raw}^{train} , D_b^{val} into D_{raw}^{val} , and D_b^{test} into D_{raw}^{test} .

The illustration in Figure 4 highlights the impact of data set splitting methods on label distribution across train, validation, and test sets. We examine the label distribution on DeepSense 6G scenario 23 data set using a beam codebook with size $M = 8$ and applying a split ratio of 65%, 15%, and 20% for training, validation, and testing, respectively. The sequential

Algorithm 1: Adjusted Splitting

```

1 function AdjustedSplit( $D_{raw}$ ,  $f_{train}$ ,  $f_{val}$ ,  $f_{test}$ ,  $P_{chunks}$ );
   Input :  $D_{raw}$ : Raw data set;
           $f_{train}$ ,  $f_{val}$ ,  $f_{test}$ : Split ratios;
           $P_{chunks}$ : Chunk size percentages;
           $M$ : Beam codebook size;
   Output:  $D_{raw}^{train}$ ,  $D_{raw}^{val}$ ,  $D_{raw}^{test}$ 

2  $N_{total} \leftarrow |D_{raw}|$ ;
3 Get label distribution  $P(b)$  from  $D_{raw}$ ;
4 Calculate chunk sizes  $C_{sizes}$  from  $P_{chunks}$ ;
5 Filter  $C_{sizes}$  based on minimum sequence length;
6  $s_{best} \leftarrow \infty$ ;
7  $D_{best}^{train}$ ,  $D_{best}^{val}$ ,  $D_{best}^{test} \leftarrow \emptyset$ ;
8 foreach chunk size  $c \in C_{sizes}$  do
9   Initialize  $D_{raw}^{train}$ ,  $D_{raw}^{val}$ ,  $D_{raw}^{test} \leftarrow \emptyset$ ;
10  Split raw data into chunks of size  $c$ ;
11  foreach chunk do
12    Split chunk into  $D_{chunk}^{train}$ ,  $D_{chunk}^{val}$ ,  $D_{chunk}^{test}$  using given
      ratios;
13     $D_{raw}^{train} \leftarrow D_{raw}^{train} \cup D_{chunk}^{train}$ ;
14     $D_{raw}^{val} \leftarrow D_{raw}^{val} \cup D_{chunk}^{val}$ ;
15     $D_{raw}^{test} \leftarrow D_{raw}^{test} \cup D_{chunk}^{test}$ ;
16  Calculate label distributions  $P_{train}(b)$ ,  $P_{val}(b)$ ,  $P_{test}(b)$  for
       $D_{raw}^{train}$ ,  $D_{raw}^{val}$ ,  $D_{raw}^{test}$ ;
17  Get distribution similarity score  $s \leftarrow \sum_{m=1}^M |P(b) - P_{train}(b)| + |P(b) - P_{val}(b)| + |P(b) - P_{test}(b)|$ ;
18  if  $s < s_{best}$  then
19     $s_{best} \leftarrow s$ ;
20     $D_{best}^{train} \leftarrow D_{raw}^{train}$ ,  $D_{best}^{val} \leftarrow D_{raw}^{val}$ ,  $D_{best}^{test} \leftarrow D_{raw}^{test}$ ;
21  $D_{raw}^{train} \leftarrow D_{best}^{train}$ ,  $D_{raw}^{val} \leftarrow D_{best}^{val}$ ,  $D_{raw}^{test} \leftarrow D_{best}^{test}$ ;
22 foreach label  $b \in \{1, \dots, M\}$  do
23    $D_b \leftarrow$  Get samples for label  $b$  from  $D_{raw}^{train}$ ,  $D_{raw}^{val}$ ,  $D_{raw}^{test}$ ;
24   Split  $D_b$  into  $D_b^{train}$ ,  $D_b^{val}$ ,  $D_b^{test}$  using given ratios;
25   Update  $D_{raw}^{train}$ ,  $D_{raw}^{val}$ ,  $D_{raw}^{test}$  with new label-based splits;
26 return  $D_{raw}^{train}$ ,  $D_{raw}^{val}$ ,  $D_{raw}^{test}$ 

```

splitting method exposes significant label distribution imbalances. Notably, the 0-th beam index presents an issue: the train data set is empty, and the test data set contains a lot of samples. In contrast, the adjusted splitting method ensures that the label distribution in each split data set reflects the label distribution of the original data set and follows the desired split ratio.

B. Data Transformation

We transform each split data set into a development data set containing U samples $D_{dev} = \{\mathcal{O}_{q,t,W,u}, \mathcal{B}_{q,t,V,u}^*\}_{u=1}^U$, which represent the model's input $\mathcal{O}_{q,t,W,u}$ and its corresponding desired output $\mathcal{B}_{q,t,V,u}^*$. The input $\mathcal{O}_{q,t,W,u}$ represents a sequence of observed sensory data $\mathcal{O}_{q,t,W,u} = \{\mathbf{O}_{q,u}[t-W+1], \dots, \mathbf{O}_{q,u}[t]\}$, where $W = 8$ and $\mathbf{O}_{q,u}[t] = \{\mathbf{g}_{UE,norm}[t], \mathbf{u}_{UE-BS}[t]\}$. The output $\mathcal{B}_{q,t,V,u}^*$ denotes the sequence of current and future beam indices $\mathcal{B}_{q,t,V,u}^* = \{b_{q,u}^*[t], \dots, b_{q,u}^*[t+V]\}$, with $V = 3$. We implement constraints to ensure the sequence integrity, requiring that the sequences $\mathcal{O}_{q,t,W,u}$ and $\mathcal{B}_{q,t,V,u}^*$ must share the same sequence index q and be ordered consecutively based on sample index t . For instance, this could manifest as an input sequence $\{\mathbf{O}_{q=1,u=1}[t-W+1], \dots, \mathbf{O}_{q=1,u=1}[t]\}$ with a corresponding

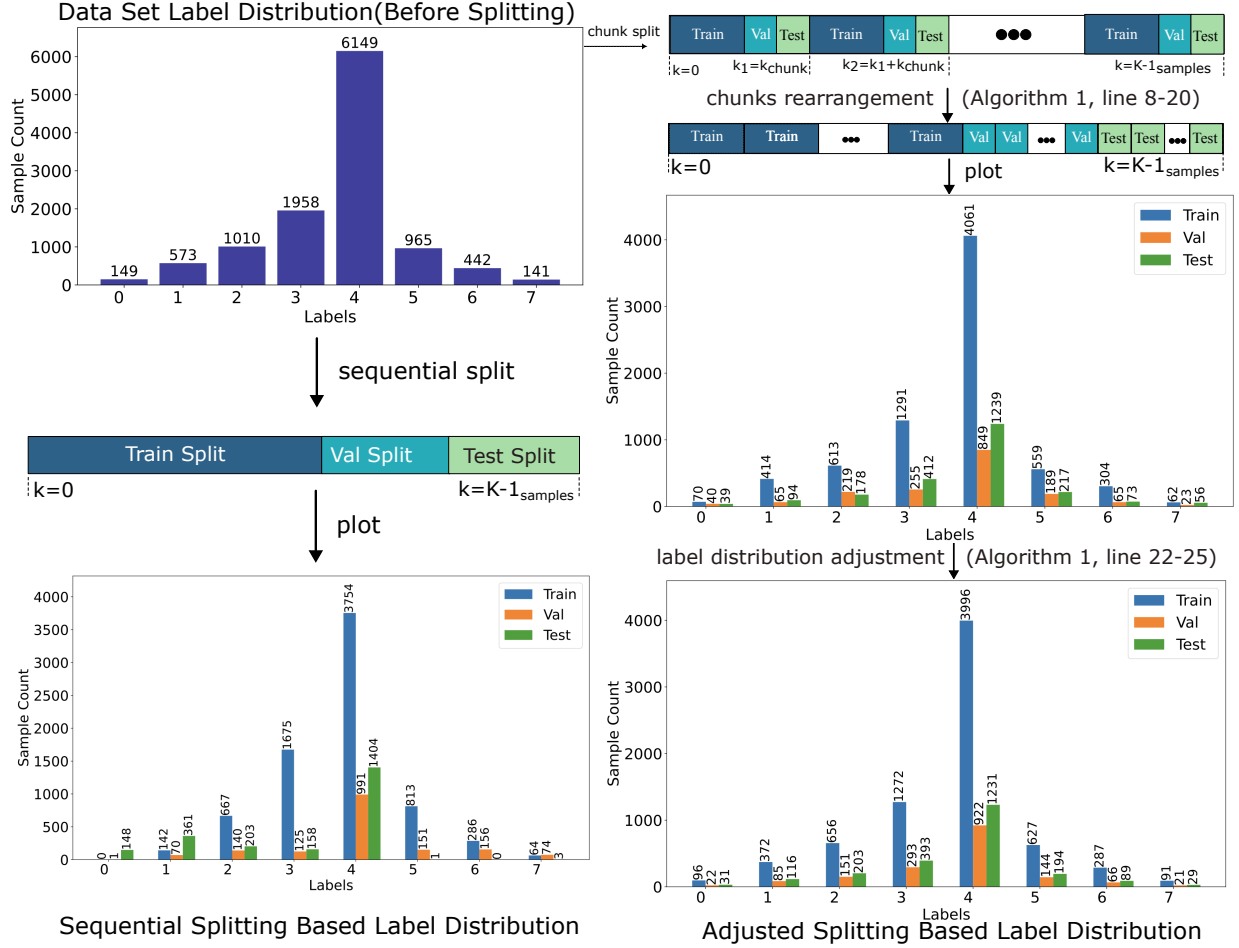


Fig. 4: Impact of data set splitting methods on label distribution across train, validation, and test sets

output $\{b_{q=1,u=1}^*[t], \dots, b_{q=1,u=1}^*[t+V]\}$. In cases where creating a perfect consecutive sequence is not possible, we implement a technique to guarantee at least $V+1$ consecutive samples with identical sequence index q . This is achieved by padding the initial $W-1$ elements of the input sequence with a zero vector \mathbf{Z} of length 5, matching the dimensions of \mathbf{O} . For instance, this method might generate an input sequence such as $\{\mathbf{Z}_{q=1,t=0,W=8,u=1}, \dots, \mathbf{Z}_{q=1,t=6,W=8,u=1}, \mathbf{O}_{q=1,t=7,W=8,u=1}\}$, while maintaining consistency in the output sequence. This strategy ensures the model is provided with well-structured inputs even when seamless continuity is unattainable. As not every sample in the raw data set D_{raw} can be arranged into these necessary sequences, the overall sample count in the development data set D_{dev} will be smaller than the total number contained in the raw data set D_{raw} (see Table II).

IV. EVALUATION RESULT

This section evaluates the proposed GPS-assisted beam prediction and tracking method using the following key metrics:

- 1) Top-K accuracy [36]: This metric quantifies the proportion of time steps across test data set samples where the beam containing Top-K confidence scores

TABLE II: Data Set Details

Data Set Type	Number of Samples	
	Sequential Splitting	Adjusted Splitting
D_{raw}^{train}	7,401 (65%)	7,387 (64.87%)
D_{raw}^{val}	1,708 (15%)	1,694 (14.88%)
D_{raw}^{test}	2,278 (20%)	2,306 (20.25%)
D_{raw}^{total}	11,387 (100%)	11,387 (100%)
D_{dev}^{train}	7,231 (65.44%)	7,093 (67%)
D_{dev}^{val}	1,609 (14.56%)	1,444 (13.64%)
D_{dev}^{test}	2,209 (20%)	2,050 (19.36%)
D_{dev}^{total}	11,049 (100%)	10,587 (100%)

encompasses the optimal beam. The Top-K accuracy is calculated as:

$$\text{Top-K accuracy} = \frac{1}{N^{test}} \sum_{l=1}^{N^{test}} \sum_{k=1}^K 1_{\{\hat{b}_{l,k}=b_l^*\}} \quad (16)$$

Here, N^{test} represents the total number of test samples, $\hat{b}_{l,k}$ is the k_{th} predicted beam index for the l -th data sample, b_l^* is the actual optimal beam index for the l -th sample, and $1_{\{\cdot\}}$ is an indicator function that returns one if the condition $\{\cdot\}$ is met.

- 2) Average Power Loss [19]: This metric assesses the average power loss between predicted and ground truth beams, mathematically expressed as:

$$P_{L[dB]} = 10 \log_{10} \left(\frac{1}{K} \sum_{k=1}^K \frac{P_{f^*}^k - 0.5P_n}{P_{\hat{f}}^k - 0.5P_n} \right), \quad (17)$$

where P_n represents the noise power of the scenario, $P_{f^*}^k$ is the power of the ground truth beam in sample k , and $P_{\hat{f}}^k$ is the power of the predicted beam for sample k . The noise power is defined as the smallest power in sample k . The noise power P_n is multiplied by half to prevent zero division in case of the predicted power $P_{\hat{f}}^k$ has equal value with noise power P_n .

- 3) Overhead Savings [19]: This metrics is defined as the reduction in training beams, are intrinsically linked to the desired reliability of the DL task. Reliability is the degree of confidence we have that a particular group of beams includes the optimal one. Higher reliability necessitates a larger beam set and consequently diminishes overhead savings. The metric $\eta_{OH}^{(90)}$, representing the overhead savings for a 90% reliability target, is calculated as $\eta_{OH}^{(90)} = 1 - \frac{b^{(90)}}{M}$, where $b^{(90)}$ denotes the minimum beams required to achieve this reliability and M is the total codebook size.
- 4) Average Power Loss Reliability: The reliability of maintaining average power loss $P_{L[dB]}$ below a threshold $P_{L[dB],threshold}$ is expressed as $R(P_{L[dB],threshold}) = \mathbb{P}(P_{L[dB]} \leq P_{L[dB],threshold})$, providing a probabilistic measure of the model's adherence to acceptable power loss margins.
- 5) Model Size: This metric is calculated by multiplying the number of non-zero model parameters (N_{params}) with a data size (Y), which is set to $Y = 32$ bits per model parameter.

A. Data Set Splitting Impact on Model Performance

In this experiment, we use concatenated normalized UE's geodetic position $\mathbf{g}_{UE,norm}$ and UE-BS unit vector \mathbf{u}_{UE-BS} as the input model but different data set splitting method. The data set details are shown in Table II. The results in Figure 5 reveal an interesting pattern regarding the impact of data set splitting methods on accuracy and power loss. For all model outputs, the adjusted splitting method achieves higher accuracy and lower power loss compared to the sequential method. The model accuracy with the adjusted splitting is about 31% ~ 34% higher than with sequential splitting for current and future beam predictions. Additionally, it achieves a power loss reduction of around 48% ~ 70% highlighting its effectiveness in enhancing model performance. These findings emphasize the importance of creating split data sets that have similar label distribution with the original data set and matches the train-validation-test split ratio of the data set to enhance model performance.

B. Model Performance Comparison

The proposed beam prediction and tracking model (with combined normalized UE's geodetic position $\mathbf{g}_{UE,norm}$ and

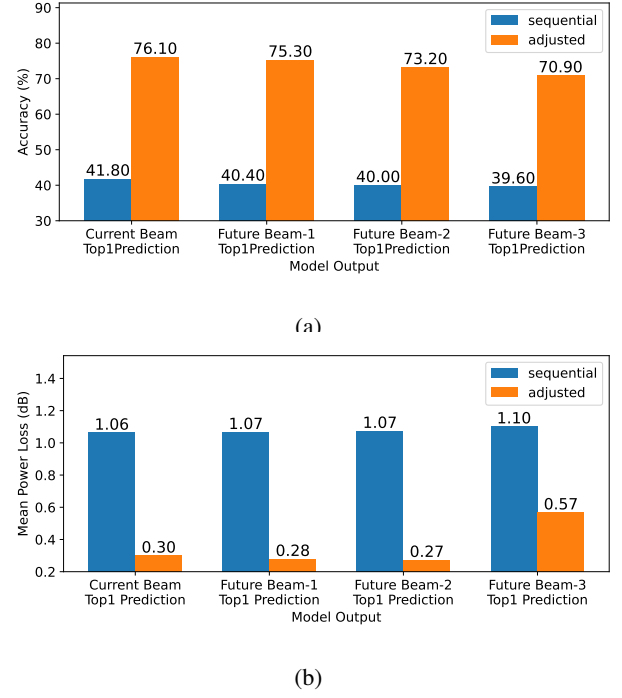


Fig. 5: Impact of data set splitting methods on (a) model accuracy and (b) model mean power loss

UE-BS unit vector \mathbf{u}_{UE-BS} inputs) has a size of 0.99 MB while delivering meaningful performance. Performance metrics, detailed in Table III, further highlight the model's performance: Top-1 accuracy consistently exceeds 70%, and Top-3 accuracy surpasses 95% across all beam prediction steps, while the mean power loss remains below 0.6 dB throughout. This low power loss indicates minimal signal degradation, even in cases where the optimal beam is not selected.

We assess the proposed model alongside baseline approaches from [28] using the same data set splitting method (adjusted data set splitting method) and the same split ratio (65% for training, 15% for validation, and 20% for testing). In comparisons with these baseline methods, the proposed model exhibits significant improvements in prediction accuracy and a marked reduction in power loss, as presented in Table III. Specifically, Top-1 accuracy increases by 7% ~ 16% across the four beam prediction steps, with the greatest improvement about 16% observed in current beam prediction. Additionally, the Top-1 mean power loss decreases by 57% ~ 69% relative to the baseline models.

Model input composition plays a critical role in the model's performance improvements, as shown in Table III. The combined approach using both normalized UE's geodetic position $\mathbf{g}_{UE,norm}$ and UE-BS unit vector \mathbf{u}_{UE-BS} inputs outperforms single-input alternatives substantially. Compared to using only normalized UE's geodetic position $\mathbf{g}_{UE,norm}$, the dual-input approach increases Top-1 prediction accuracy by 8% ~ 11.6% across all prediction steps while decreasing mean power loss by 53% ~ 69%. Similarly, when compared to using only UE-BS vector \mathbf{u}_{UE-BS} input, the combined approach yields

TABLE III: Comparison of model performance metrics across different model architecture and input

Model	Input	Size (MB)	Current Beam Prediction			Future Beam-1 Prediction			Future Beam-2 Prediction			Future Beam-3 Prediction		
			Top-1 Acc. (%)	Top-3 Acc. (%)	Top-1 Mean Power Loss (dB)	Top-1 Acc. (%)	Top-3 Acc. (%)	Top-1 Mean Power Loss (dB)	Top-1 Acc. (%)	Top-3 Acc. (%)	Top-1 Mean Power Loss (dB)	Top-1 Acc. (%)	Top-3 Acc. (%)	Top-1 Mean Power Loss (dB)
Baseline Beam Prediction	$\mathbf{g}_{UE,norm}$	1.07	60	87.5	0.822	-	-	-	-	-	-	-	-	-
Baseline Beam Tracking	$\mathbf{g}_{UE,norm}$	0.59	-	-	-	63.9	88.7	0.905	63.9	89.9	1.068	63.2	89.6	1.348
Proposed Beam Prediction & Tracking	$\mathbf{g}_{UE,norm}$	0.99	64.8	89.8	0.726	63.7	90.3	0.805	63.4	89.7	0.889	62.5	88.2	1.224
Proposed Beam Prediction & Tracking	\mathbf{u}_{UE-BS}	0.99	62.1	94.2	0.953	61.3	94.8	0.862	59.3	94.9	0.819	57.5	92.9	1.077
Proposed Beam Prediction & Tracking	$\{\mathbf{g}_{UE,norm}, \mathbf{u}_{UE-BS}\}$	0.99	76.1	97.3	0.299	75.3	97.8	0.278	73.2	97.4	0.272	70.9	95.3	0.567

13% ~ 14% improvements in Top-1 accuracy and reduces mean power loss by 47% ~ 68%. These results demonstrate that integrating spatial information from both the UE position and its directional relationship with the BS creates a more comprehensive context for the model to make accurate beam predictions.

C. Model Performance Accross Various UAV Height

Figure 6 (a) displays the accuracy of the proposed model across different height categories, while Figure 6 (b) illustrates the data set distribution across the training, validation, and test sets. The model excels in the high height category, with accuracy spanning from about 73.9% to 80.6% across all beam prediction steps, possibly reflecting its strong representation in the data set (4,836 training samples). The low height category, despite having the smallest training sample size (31 samples), achieves a moderate accuracy range of 66.1% to 76.8% across all prediction steps. Meanwhile, the medium height category demonstrates the lowest accuracy, ranging from 65.3% to 71.2% across all steps. To assess model performance independent of data set distribution, we analyzed it using an equal sample size (56 samples, sampled 20 times from the test data set) across all height categories, as detailed in Table IV. The table indicates that the high height category achieves the highest mean accuracy range (71.88% to 79.55%), followed by the low (66.07% to 76.79%) and medium categories (65.18% to 73.39%) across all prediction steps. This trend implies that accuracy does not increase linearly with flight height and highlights medium heights as the most challenging category.

Figure 6 (c) illustrates the mean power loss across height categories for both current and future beam predictions. For current beam predictions, the medium height category exhibits the highest mean power loss (0.49 dB), followed by low height category (0.46 dB) and high height category (0.19 dB). In future beam predictions, the medium height category continues to show the highest mean power loss range (0.3 dB to 1.16 dB), with high height category (0.23 dB to 0.27 dB) and low height category (0.06 dB to 0.16 dB) following. This suggests that medium heights consistently suffer the largest mean power

loss across all prediction steps. This finding aligns with the medium height category having the highest average power value (0.480), as depicted in Figure 6 (d). A higher average power loss indicates a wider spread of power across beam indices, which elevates noise power. According to equation 17, an increase in noise power narrows the gap between predicted power and noise power, resulting in a higher mean power loss. Overall, the pattern reveals that medium heights consistently face greater power loss challenges, driven by increased noise due to power distribution.

D. Model performance across various UAV speeds

Figure 7 (a) illustrates the Top-1 prediction accuracy of the proposed model across speed categories, while Figure 7 (b) presents the corresponding data set distribution across the training, validation, and test sets. The model achieves the highest accuracy in the slow speed category, ranging from approximately 75.7% to 80.3% for all beam prediction steps. This may align with its dominant representation in the data set (4,336 samples in the training set). The medium speed category shows a lower accuracy varying between 64.5% and 71.4% across all prediction steps. The fast speed category exhibits the lowest accuracy, ranging from 55.6% to 65.3% across all prediction steps, despite having similar sample sizes to the medium category (1,418 and 1,339 in the training set for medium and fast categories, respectively). This trend suggests that while the larger data set size for the slow category may contribute to its higher accuracy, the prediction accuracy steadily decreases as speed increases. Moreover, despite the fast category having a similar amount of data as the medium category, its accuracy drops significantly, indicating that higher speeds introduce prediction challenges not solely attributable to low data samples.

Figure 7 (c) depicts the mean power loss across speed categories for current and future beam predictions, while Figure 7 (d) shows the centered power footprint on the test data set, with average power values of 0.366 for slow, 0.529 for medium, and 0.620 for fast speed categories. In the slow speed category, the mean power loss is low, varying



Fig. 6: Model Performance on Various UAV Height

TABLE IV: Model Performance on Various UAV Height with Equal Number of Samples

Height Category	Number of Samples	Sampling Rounds	Current Prediction Top1 Acc (%)	Future Prediction 1 Top1 Acc (%)	Future Prediction 2 Top1 Acc (%)	Future Prediction 3 Top1 Acc (%)
Low(≤ 40 m)	56	20	76.79 \pm 0.00	75.00 \pm 0.00	66.07 \pm 0.00	69.64 \pm 0.00
Medium(40~80 m)	56	20	69.29 \pm 6.10	73.39 \pm 5.59	69.38 \pm 4.53	65.18 \pm 5.66
High(> 80 m)	56	20	79.55 \pm 3.89	76.52 \pm 4.46	74.91 \pm 6.38	71.88 \pm 7.18

between 0.11 dB and 0.15 dB, and the power footprint is more concentrated at the center with little variation across beam indices, showing that the beam prediction and tracking remains steady and performs reliably. For the medium speed category, the mean power loss increases to a range of 0.3 dB to 0.7 dB, with a wider footprint that fluctuates more, suggesting some difficulty in keeping performance stable. Meanwhile, the fast speed category experiences the highest power loss, from 0.71 dB to 2.19 dB, and its footprint is the most spread out, with noticeable beam peaks, which points to significant challenges in accurately predicting and tracking beams at higher speeds. The trend of higher mean power loss paired with a more spread-out power footprint highlights how speed affects both the model's performance and the shape of the power distribution, with faster speeds resulting in larger power losses and wider power footprint.

E. Training Overhead Savings and Mean Power Loss Reliability

Figure 8 (a) demonstrates how beam prediction and tracking model reduces training overhead across different reliability levels. At 80% guaranteed reliability, the model achieves approximately 95% overhead savings, meaning that with a codebook size of 32 classes, only 1 ~ 2 beams need training instead of all 32. When the reliability threshold is elevated to 99%, the model still sustains a 89% overhead savings, necessitating the training of merely 3 ~ 4 beams. This result highlight the model capability in reducing beam training overhead.

Figure 8 (b) analyzes the mean power loss reliability across four beam prediction steps, focusing on 1 dB and 3 dB thresholds. When considering the stricter 1 dB threshold, which represents a 20% power loss, the reliability across all prediction steps falls within a robust range of 94.3% to 95.7%. Moreover, when the threshold is relaxed to 3 dB, signifying a



Fig. 7: Model Performance on Various UAV Speed

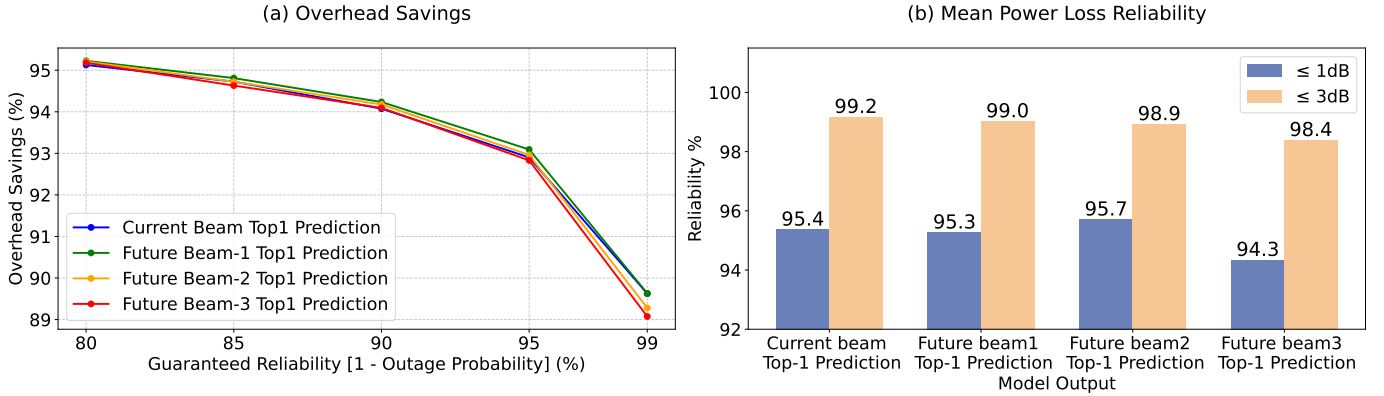


Fig. 8: Model overhead savings and mean power loss reliability

50% power reduction, the reliability across all prediction steps demonstrates higher values, ranging from 98.4% to 99.2%. This result highlights the model's capability in maintaining high power loss reliability, particularly at less demanding thresholds.

F. Model Performance Across Different Beam Codebook Sizes

Figure 9 evaluates model performance across beam codebook sizes (8, 16, 32, and 64 beams). Figure 9(a) reveals that smaller codebooks deliver higher beam prediction accuracy, with 8 beams achieving a range of 85% \sim 88% and 16 beams

ranging from 84% to 86% for both current and future beam predictions, with the current beam prediction using 8 beams achieving the peak accuracy of 88.00%. However, accuracy declines notably with larger codebooks, starting with 32 beams where accuracy drops to a range of 70% \sim 76% across current and future predictions, and further decreasing to a range of 63% \sim 64% for 64 beams. The trend indicates that smaller beam codebook sizes consistently outperform larger ones in terms of prediction accuracy.

Figure 9(b) illustrates the mean power loss for both current and future beam predictions across varying codebook sizes.

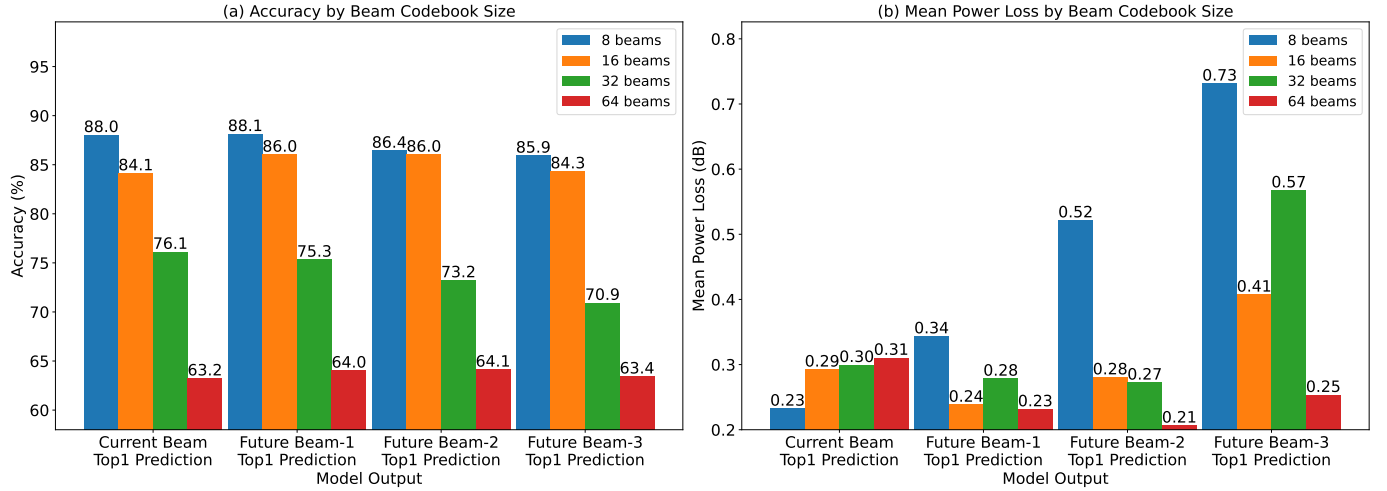


Fig. 9: Model Performance on Various Beam Codebook Size

For current beam predictions, the mean power loss exhibits an upward trend, climbing from 0.23 dB in the 8-beam model to 0.31 dB in the 64-beam model. In the 8-beam model specifically, the mean power loss steadily increases with each prediction step, peaking at 0.73 dB for the third future beam prediction. The data reveals that while mean power loss in current beam predictions consistently grows with larger codebook sizes, future beam predictions show greater variability. Nevertheless, across all prediction steps, the mean power loss remains under 0.8 dB.

V. CONCLUSION

This study introduces a GPS-aided DL model capable of simultaneous prediction of both present and future beams for mmWave UAV communication, demonstrating performance with Top-1 accuracy exceeding 70% and mean power loss below 0.6 dB throughout all temporal prediction steps. The results are driven by a data set splitting strategy that ensures even label distribution, combined with a GPS preprocessing method that captures essential positional features, and a DL architecture that converts sequential position data into beam index predictions. The adjusted splitting approach outperforms sequential methods by 31% ~ 34% in accuracy while reducing mean power loss by 48% ~ 70%. The combined feature approach—integrating normalized UE geodetic position with UE-BS unit vector—consistently delivers superior performance, improving Top-1 Accuracy by 8% ~ 11.6% and decreasing mean power loss by 53% ~ 69% compared to using only normalized UE geodetic position. Similar advantages (13% ~ 14% higher accuracy, 47% ~ 68% lower mean power loss) are observed over the model using only UE-BS unit vector input. Furthermore, the proposed model achieves 93% overhead savings (requiring the training of 2 ~ 3 beams instead of 32 beams) while achieving beam prediction accuracy guarantees of 95%. The model demonstrates reliable performance with 94% ~ 96% of predictions maintaining power loss within 1 dB. Future research could aim to enhance the performance of the GPS-based model for UAVs operating

at medium altitudes (40 m ~ 80 m) and high speeds (>20 mph).

REFERENCES

- [1] Y. Zeng, Q. Wu, and R. Zhang, "Accessing From the Sky: A Tutorial on UAV Communications for 5G and Beyond," *Proceedings of the IEEE*, vol. 107, no. 12, pp. 2327–2375, Dec. 2019.
- [2] Z. Xiao, L. Zhu, Y. Liu, P. Yi, R. Zhang, X.-G. Xia, and R. Schober, "A Survey on Millimeter-Wave Beamforming Enabled UAV Communications and Networking," *IEEE Communications Surveys & Tutorials*, vol. 24, no. 1, pp. 557–610, 2022.
- [3] G. Geraci, A. Garcia-Rodriguez, M. M. Azari, A. Lozano, M. Mezzavilla, S. Chatzinotas, Y. Chen, S. Rangan, and M. D. Renzo, "What Will the Future of UAV Cellular Communications Be? A Flight From 5G to 6G," *IEEE Communications Surveys & Tutorials*, vol. 24, no. 3, pp. 1304–1335, 2022.
- [4] Q. Xue, C. Ji, S. Ma, J. Guo, Y. Xu, Q. Chen, and W. Zhang, "A Survey of Beam Management for mmWave and THz Communications Towards 6G," *IEEE Communications Surveys & Tutorials*, pp. 1–1, 2024.
- [5] C. Zhang, W. Zhang, W. Wang, L. Yang, and W. Zhang, "Research Challenges and Opportunities of UAV Millimeter-Wave Communications," *IEEE Wireless Communications*, vol. 26, no. 1, pp. 58–62, Feb. 2019.
- [6] M. Giordani, M. Polese, A. Roy, D. Castor, and M. Zorzi, "A Tutorial on Beam Management for 3GPP NR at mmWave Frequencies," *IEEE Communications Surveys & Tutorials*, vol. 21, no. 1, pp. 173–196, 2019.
- [7] W. Yi, W. Zhiqing, and F. Zhiyong, "Beam training and tracking in mmWave communication: A survey," *China Communications*, vol. 21, no. 6, pp. 1–22, Jun. 2024.
- [8] K. Chen and C. Qi, "Beam Training Based on Dynamic Hierarchical Codebook for Millimeter Wave Massive MIMO," *IEEE Communications Letters*, vol. 23, no. 1, pp. 132–135, Jan. 2019.
- [9] C. Qi, K. Chen, O. A. Dobre, and G. Y. Li, "Hierarchical Codebook-Based Multiuser Beam Training for Millimeter Wave Massive MIMO," *IEEE Transactions on Wireless Communications*, vol. 19, no. 12, pp. 8142–8152, Dec. 2020.
- [10] A. Alkhateeb, O. El Ayach, G. Leus, and R. W. Heath, "Channel Estimation and Hybrid Precoding for Millimeter Wave Cellular Systems," *IEEE Journal of Selected Topics in Signal Processing*, vol. 8, no. 5, pp. 831–846, Oct. 2014.
- [11] Y. Han and J. Lee, "Two-stage compressed sensing for millimeter wave channel estimation," in *2016 IEEE International Symposium on Information Theory (ISIT)*, Jul. 2016, pp. 860–864.
- [12] A. Alkhateeb, S. Alex, P. Varkey, Y. Li, Q. Qu, and D. Tujkovic, "Deep Learning Coordinated Beamforming for Highly-Mobile Millimeter Wave Systems," *IEEE Access*, vol. 6, pp. 37 328–37 348, 2018.
- [13] J. Liu, X. Li, T. Fan, S. Lv, and M. Shi, "Multimodal Fusion Assisted Mmwave Beam Training in Dual-Model Networks," *IEEE Transactions on Vehicular Technology*, vol. 73, no. 1, pp. 995–1011, Jan. 2024.
- [14] X. Xin and Y. Yang, "Robust Beam Tracking with Extended Kalman Filtering for Mobile Millimeter Wave Communications," in *2019 Com-*

- puting, *Communications and IoT Applications (ComComAp)*, Oct. 2019, pp. 172–177.
- [15] S. G. Larew and D. J. Love, “Adaptive Beam Tracking With the Unscented Kalman Filter for Millimeter Wave Communication,” *IEEE Signal Processing Letters*, vol. 26, no. 11, pp. 1658–1662, Nov. 2019.
- [16] Y. Ke, H. Gao, W. Xu, L. Li, L. Guo, and Z. Feng, “Position Prediction Based Fast Beam Tracking Scheme for Multi-User UAV-mmWave Communications,” in *ICC 2019 - 2019 IEEE International Conference on Communications (ICC)*, May 2019, pp. 1–7.
- [17] W. Yuan, C. Liu, F. Liu, S. Li, and D. W. K. Ng, “Learning-Based Predictive Beamforming for UAV Communications With Jittering,” *IEEE Wireless Communications Letters*, vol. 9, no. 11, pp. 1970–1974, Nov. 2020.
- [18] C. Liu, W. Yuan, Z. Wei, X. Liu, and D. W. K. Ng, “Location-Aware Predictive Beamforming for UAV Communications: A Deep Learning Approach,” *IEEE Wireless Communications Letters*, vol. 10, no. 3, pp. 668–672, Mar. 2021.
- [19] J. Morais, A. Bchboodi, H. Pezeshki, and A. Alkhateeb, “Position-Aided Beam Prediction in the Real World: How Useful GPS Locations Actually are?” in *ICC 2023 - IEEE International Conference on Communications*, May 2023, pp. 1824–1829.
- [20] S. Jiang, G. Charan, and A. Alkhateeb, “LiDAR Aided Future Beam Prediction in Real-World Millimeter Wave V2I Communications,” *IEEE Wireless Communications Letters*, vol. 12, no. 2, pp. 212–216, Feb. 2023.
- [21] G. Charan, T. Osman, A. Hredzak, N. Thawdar, and A. Alkhateeb, “Vision-Position Multi-Modal Beam Prediction Using Real Millimeter Wave Datasets,” in *2022 IEEE Wireless Communications and Networking Conference (WCNC)*. Austin, TX, USA: IEEE, Apr. 2022, pp. 2727–2731.
- [22] H. Luo, U. Demirhan, and A. Alkhateeb, “Millimeter Wave V2V Beam Tracking using Radar: Algorithms and Real-World Demonstration,” in *2023 31st European Signal Processing Conference (EUSIPCO)*, Sep. 2023, pp. 740–744.
- [23] S. Jiang and A. Alkhateeb, “Computer Vision Aided Beam Tracking in A Real-World Millimeter Wave Deployment,” in *2022 IEEE Globecom Workshops (GC Wkshps)*, Dec. 2022, pp. 142–147.
- [24] G. Charan, A. Hredzak, C. Stoddard, B. Berrey, M. Seth, H. Nunez, and A. Alkhateeb, “Towards Real-World 6G Drone Communication: Position and Camera Aided Beam Prediction,” in *GLOBECOM 2022 - 2022 IEEE Global Communications Conference*, Dec. 2022, pp. 2951–2956.
- [25] G. Charan, A. Hredzak, and A. Alkhateeb, “Millimeter Wave Drones with Cameras: Computer Vision Aided Wireless Beam Prediction,” in *2023 IEEE International Conference on Communications Workshops (ICC Workshops)*, May 2023, pp. 1896–1901.
- [26] I. Ahmad, A. R. Khan, R. N. B. Rais, A. Zoha, M. A. Imran, and S. Hussain, “Vision-Assisted Beam Prediction for Real World 6G Drone Communication,” in *2023 IEEE 34th Annual International Symposium on Personal, Indoor and Mobile Radio Communications (PIMRC)*, Sep. 2023, pp. 1–7.
- [27] Z. Zarei, F. D. Tilahun, and C. G. Kang, “Vision-assisted Beam Prediction for UAV-enabled Millimeter-Wave Communications using SE-ResNet50,” in *2023 14th International Conference on Information and Communication Technology Convergence (ICTC)*, Oct. 2023, pp. 1659–1661.
- [28] G. Charan and A. Alkhateeb, “Sensing-Aided 6G Drone Communications: Real-World Datasets and Demonstration,” Dec. 2024. [Online]. Available: <http://arxiv.org/abs/2412.04734>
- [29] A. Alkhateeb, G. Charan, T. Osman, A. Hredzak, J. Morais, U. Demirhan, and N. Srinivas, “DeepSense 6G: A Large-Scale Real-World Multi-Modal Sensing and Communication Dataset,” *IEEE Communications Magazine*, vol. 61, no. 9, pp. 122–128, Sep. 2023.
- [30] W. Dong, J. Li, R. Yao, C. Li, T. Yuan, and L. Wang, “Characterizing Driving Styles with Deep Learning,” Oct. 2016. [Online]. Available: <http://arxiv.org/abs/1607.03611>
- [31] M. K. Paul, “A note on computation of Geodetic coordinates from geocentric (Cartesian) coordinates,” *Bulletin géodésique*, vol. 108, no. 1, pp. 135–139, Jun. 1973.
- [32] J. Zhu, “Conversion of Earth-centered Earth-fixed coordinates to geodetic coordinates,” *IEEE Transactions on Aerospace and Electronic Systems*, vol. 30, no. 3, pp. 957–961, Jul. 1994.
- [33] A. O. Ige and M. Sibiya, “State-of-the-Art in 1D Convolutional Neural Networks: A Survey,” *IEEE Access*, vol. 12, pp. 144 082–144 105, 2024.
- [34] K. Cho, B. Van Merriënboer, C. Gulcehre, D. Bahdanau, F. Bougares, H. Schwenk, and Y. Bengio, “Learning Phrase Representations using RNN Encoder–Decoder for Statistical Machine Translation,” in *Proceedings of the 2014 Conference on Empirical Methods in Natural Language Processing (EMNLP)*. Doha, Qatar: Association for Computational Linguistics, 2014, pp. 1724–1734.
- [35] J. Chung, C. Gulcehre, K. Cho, and Y. Bengio, “Empirical Evaluation of Gated Recurrent Neural Networks on Sequence Modeling,” Dec. 2014. [Online]. Available: <http://arxiv.org/abs/1412.3555>
- [36] Y. Yeo and J. Kim, “Multi-Modal Sensing-Aided Beam Prediction using Poolformer for UAV Communications,” in *2024 Fifteenth International Conference on Ubiquitous and Future Networks (ICUFN)*, Jul. 2024, pp. 202–204.